Hindawi
Journal of Sensors
Volume 2022, Article ID 7087679, 18 pages
https://doi.org/10.1155/2022/7087679

*Research Article*

# Research on Cavitation Flow Dynamics and Entropy Generation Analysis in an Axial Flow Pump

**Simin Shen**,[1,2,3] **Bensheng Huang**,[1] **Si Huang**,[3] **Shun Xu**,[4] **and Shufeng Liu**[1]

[1]*Guangdong Research Institute of Water Resources and Hydropower, Guangzhou 510610, China*
[2]*School of Water Resources and Hydropower Engineering, Wuhan University, Wuhan 430072, China*
[3]*School of Mechanical and Automotive Engineering, South China University of Technology, Guangzhou 510641, China*
[4]*School of Aerospace Engineering, Huazhong University of Science and Technology, Wuhan 430074, China*

Correspondence should be addressed to Simin Shen; emilyfluent@126.com

Received 21 March 2022; Accepted 24 May 2022; Published 22 June 2022

Academic Editor: Haidong Shao

Copyright © 2022 Simin Shen et al. This is an open access article distributed under the Creative Commons Attribution License, which permits unrestricted use, distribution, and reproduction in any medium, provided the original work is properly cited.

The entropy generation theory is introduced to investigate the effects of different NPSH and tip clearance size on the cavitation flow dynamics and mechanical energy dissipation intuitively and quantitatively within an axial flow pump through numerical simulations. The results indicate that main mechanical energy dissipation of the pump gathers in part impeller and diffuser, and most are turbulent dissipation. Meanwhile, the impeller is the largest place of mechanical energy dissipation of the pump under cavitation conditions, accounting for more than 50%. NPSH has significant effects on the cavitation pattern, which reflects on the field that the areas of attached sheet cavitation and tip leakage vortex cavitation around blades increase obviously with NPSH reducing under the tip clearance of 0.1% span. With NPSH decreasing, high regions of turbulent dissipation in the impeller mainly expands along blades and move downstream, with span S0.98 near the shroud having larger turbulent dissipation. Besides, high regions of turbulent dissipation are mainly distributed at the rear part of the cavity for every corresponding span of the impeller, which indicates that the turbulent dissipation has a strong relation with the cavitation pattern. In the impeller, the unstable flows cause cavity shedding at the rear of the cavity and wake flows near the blade trail induce higher turbulent kinetic energy, finally resulting in higher turbulent dissipation there. Under the same NPSH, areas of tip leakage vortex cavitation and areas of tip clearance cavitation around the tip both expand with the tip clearance increasing from 0.1% span to 0.8% span. And high areas of turbulent dissipation also are distributed at the rear of the cavity and moving downstream along the blade suction side, especially at span S0.98. Therefore, the tip clearance width mainly affects the cavitation development and turbulent dissipation distribution near the impeller's shroud under same NPSH.

## 1. Introduction

It is well known that axial-flow pumps are widely used in hydraulic engineering projects like agricultural irrigation, water supply, and drainage. The cavitation in hydraulic machinery is an important phenomenon of complex phase change, which often occurs where local pressure is lower than liquid vaporization pressure. Due to the existence of radial clearance between blades and the shroud for the impeller, tip leakage flows would occur inevitably and cause the tip leakage vortex cavitation cloud under the cavitation conditions, which finally makes the cavitation process more complicated. When the cavitation is severe, it can influence the flow structure and energy loss characteristic, then finally result in vibration, noise, and the deterioration of hydraulic machinery performance [1–4].

Currently, the two common methods to study the cavitation dynamics in hydraulic machinery are through experiments and numerical simulations. As for the study on the cavitation inside axial-flow pumps, several scholars investigate the cavitation combined the experiment with the numerical simulation. Saito [5] investigated the flow pattern under cavitation conditions within an axial-flow impeller and found that the change of pump performance has a close relation with cavitation growth around blades. Due to the cavitation, the flow pattern at the impeller outlet changed

remarkably. Zhang and Chen [6] investigated the inner flows in a slanted axial pump with different cavitation conditions by numerical simulations. The research introduced boundary vorticity flux to diagnose the cavitation flow and found the decrease of cavitation performance had a relation with unstable cavitation flows on the suction sides of blades. Hosono et al. [7] studied the internal flow and the influence of the cavitation within an axial pump by measurements through the high-speed camera and numerical simulations. Shi et al. [8] studied effects of different blade tip geometries on the cavitation and leakage vortex for an axial pump. Zhang et al. [9, 10] investigated the internal flow by CFD method to investigate the tip flow cavitation patterns of a pump. They found the phenomenon that tip leakage vortex-(TLV-) induced periodically collapse of perpendicular vortices is universal for axial flow pumps. Tan et al. [11] applied high-speed imaging to investigate some forms of cavitation patterns like sheet cavitation and tip clearance cavitation under varying discharge for a pump. Feng et al. [12] investigated impacts of inlet guide vane on the cavitation dynamics and pump performance with varying discharge. They found a variable called the total vapor fraction to predict critical net positive suction head. Also, many scholars [13–22] carried out the research on the tip leakage vortex, pressure pulsation, and cavitation mechanism fields in hydraulic machinery and obtained a certain number of achievements, while for studies on energy loss characteristics in hydraulic machinery, an increasing number of scholars use the entropy production method to investigate the loss characteristic accompany with the numerical simulation. Comparing with traditional energy evaluation method, entropy generation analysis method can intuitively and quantitatively determine the position of mechanical energy dissipation in hydraulic machinery; thus, this method is currently applied by some researchers. Gong et al. [23] investigated energy dissipation of a hydroturbine by entropy generation analysis, and they found the runner and guide vane were mainly locations of energy loss. Li et al. [24, 25] investigated hysteresis characteristics using entropy generation analysis of a pump-turbine model by simulations. Through analysis, they found that the hump characteristic was induced by the energy dissipation of the runner. Hou et al. [26] introduced the entropy production theory to investigate energy dissipation in pumps. Pei et al. [27] conducted the research of energy dissipation applying entropy generation analysis in a pump with varying distance between the guide vane and impeller. Chang et al. [28] applied the entropy generation method to investigate effects of the blade thickness distribution on losses in novel self-priming pump and obtained optimal blade. Li et al. [29] introduced entropy generation theory to investigate about the cavitation and loss characteristic in a centrifugal pump. From their simulation results, they found the decrease of pump head is related to the change of overall entropy production rate of part impeller. Wang et al. [30] applied entropy production diagnostic model (EPDM) to study energy dissipation under cavitation conditions in a pump, and they proved that the EPDM can predict the inception and development of the cavitation. Some studies [31–34] investigated the inner flow and energy dissipation based on entropy generation theory in hydraulic machinery and get some results. These above studies about energy loss characteristics in hydraulic machinery prove the entropy generation method is effective to assess mechanical energy dissipation due to its intuitive and quantitative advantages.

The above studies are about cavitation dynamics or about loss characteristics of hydraulic machines using entropy generation method, while there is still few studies on the relations between the cavitation dynamics and entropy production for axial-flow pumps, especially with different NPSH and tip clearance. The main focus of this research is to investigate cavitation dynamics and entropy generation analysis of an axial-flow pump with different NPSH and tip clearance width and found the relations between the cavitation and entropy production. Therefore, four NPSH with the same tip clearance of 0.1% span are selected to investigate effects of NPSH on cavitation flows and energy dissipation, while four tip clearance widths with the same cavitation condition are selected to investigate impacts of the tip clearance on cavitation patterns and energy dissipation. That is how this research organized. Then, we summarize some conclusions about cavitation dynamics and mechanical energy dissipation for an axial-flow pump. This research can finally provide some theoretical guidance to the cavitation and energy dissipation in hydraulic machinery and give reference for designing highly reliable pumps.

## 2. Experimental Apparatus and Parameters

As shown in Figure 1, the closed experimental loop is installed at the Laboratory of Pump Station in Wuhan University, Wuhan, China [14]. The experimental apparatus mainly consists of three parts: the axial-flow pump facility, the cavitation generating facility, and the data acquisition system. The test pump loop includes water tanks, a flowmeter, valves, an axial flow pump, and other related equipment displayed in Figure 2. Specific parameters for the experimental model are given in Table 1. The cavitation generating facility mainly contains a vacuum pump, a pressure tank, and a regulating valve. During the experiment, the inlet pressure of test pump is maintained by a vacuum pump through adjusting the regulating valve to different required degrees of vacuum. The data acquisition system consists of pressure sensors, the electromagnetic flowmeter, and speed torque meter. The electromagnetic valve controls the mass flow rate. And the KROHNE electromagnetic flowmeter measures the mass flow (accuracy 0.3%). While a frequency converter controls the pump rotation speed and torque. And the WDH300Z speed torque meter measures these parameters (accuracy 0.2%). The WDHYL101 pressure sensors measure the inlet and outlet pressure of test pump (accuracy 0.2%). To avoid accidental errors, repeated measurements are performed for every working condition. Comparing the results of 3, 5, and 10 times, it was found that the average values of five measurements were enough for this test. During the measurements, the uncertainties of mass flow rate, head,


Figure 1: Experimental pump station installed in the Wuhan University.

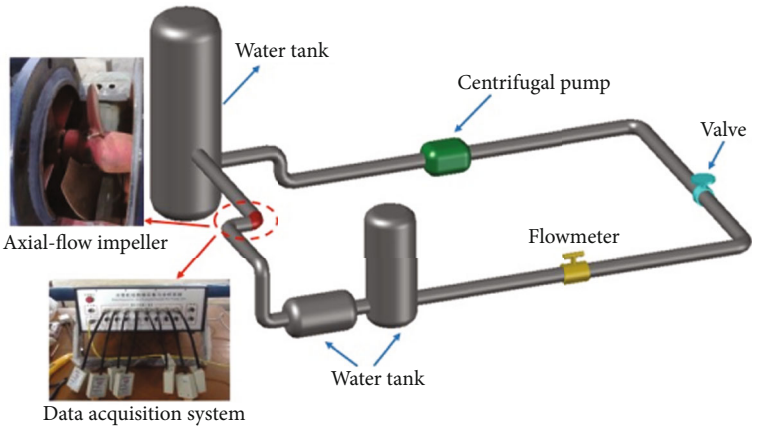


Figure 2: Schematic of test pump.

input power, and efficiency were less than 0.84%, 0.58%, 0.75%, and 1.01%, respectively.

## 3. Physical Modelling and Numerical Methodology

*3.1. Governing Equations, Turbulence Model, and Cavitation Model.* For the cavitation flow under isothermal conditions, a homogeneous mixture model has been applied in a wide range of numerical calculations. The homogeneous mixing model assumes the velocity and pressure between the liquid phase and gas phase are continuous. Governing equations for cavitation flows accompany with the homogeneous mixture model include continuity and momentum equations, which can be expressed as:

$$\frac{\partial \rho_m}{\partial t} + \frac{\partial (\rho_m u_i)}{\partial x_i} = 0, \tag{1}$$

$$\frac{\partial (\rho_m u_i)}{\partial t} + \frac{\partial (\rho_m u_i u_j)}{\partial x_j} = -\frac{\partial p}{\partial x_i} + \frac{\partial}{\partial x_j}\left[(\mu_{0+}\mu_m)\right]\left(\frac{\partial u_i}{\partial x_j} + \frac{\partial u_j}{\partial x_i}\right), \tag{2}$$

where $p$ is the pressure; $u$ is the velocity; $\rho_m$ denotes mixture phase density and can be defined by Equation (3); $\mu_0$ represents mixture laminar viscosity, which can be calculated by Equation (4); and $\mu_m$ denotes mixture turbulent viscosity and can be acquired by adopting turbulence model. Because the SST $k$-$\omega$ turbulence model can effectively predict flow separation and vortexes with adverse pressure gradients in hydraulic machinery, the governing equations are solved by SST $k$-$\omega$ turbulence model in current study.

Table 1: Specific parameters of test pump.

| Parameters | Value |
|---|---|
| Impeller diameter $D$ (mm) | 300 |
| Number of diffuser blades | 5 |
| Number of impeller blades | 3 |
| Design rotational speed $n$ (r/min) | 1450 |
| Design head $H_d$ (m) | 3.3 |
| Design flow rate $Q_d$ (kg/s) | 330 |
| Tip clearance (mm) | 0.15 |

$$\rho_m = \alpha_v \rho_v + (1 - \alpha_v)\rho_1, \tag{3}$$

$$\mu_0 = \alpha_v \mu_v + (1 - \alpha_v)\mu_1, \tag{4}$$

$$\alpha_v + \alpha_1 = 1, \tag{5}$$

where $\alpha_v$ is volume fraction of vapor; subscripts $m$, $l$, and $v$ represent mixing, liquid, and vapor phases, respectively. The vapor transport equation can solve the volume fraction of water vapor, the equation is:

$$\frac{\partial(\rho_v\alpha_v)}{\partial t} + \frac{\partial\left(\rho_v\alpha_v u_j\right)}{\partial x_j} = \dot{m}^+ + \dot{m}^-, \tag{6}$$

where $\dot{m}^+$ is the evaporation source term; $\dot{m}^-$ is condensation source term. This study adopts Zwart-Gerber-Belamri cavitation model to express mass exchange of interphase; thus, $\dot{m}^+$ and $\dot{m}^-$ can be defined as:

$$\dot{m}^+ = F_{va}\frac{3\alpha_c(1-\alpha_v)\rho_v}{R_b}\sqrt{\frac{2|p_v - p|}{3\rho_1}}, \tag{7}$$

$$\dot{m}^- = F_{co}\frac{3\alpha_v\rho_v}{R_b}\sqrt{\frac{2|p_v - p|}{3\rho_1}}, \tag{8}$$

where $F_{va}$ and $F_{co}$ represent the empirical coefficient of evaporation and condensation, respectively; $p_v$ denotes saturated vapor pressure; $R_b$ stands for the bubble radius; and $\alpha_c$ represents nucleation site volume fraction. The recommended values for parameters are $F_{va} = 50$, $F_{co} = 0.01$, $R_b = 1 \times 10^{-6}$ m, and $\alpha_c = 5 \times 10^{-4}$.

*3.2. Entropy Generation Calculation Equations.* In current research, the entropy generation analysis is used to assess mechanical energy dissipation within an axial flow pump. According to the second law of thermodynamics, entropy generation refers to irreversible energy losses in the energy conversion process. Regarding the internal fluid of a pump as an incompressible and adiabatic process, entropy generation created by heat transfer could be ignored. Therefore, mechanical energy dissipation within the flow passage of a pump mainly is viscous and turbulent dissipation. And local entropy generation rate caused by dissipation for cavitation flows is written as $\bar{\Phi}/T$, which can be defined directly as:

$$\frac{\bar{\Phi}}{T} = \dot{S}''_{\bar{D}} + \dot{S}''_{D'}, \tag{9}$$

where $\dot{S}''_{\bar{D}}$ and $\dot{S}''_{D'}$ represent the entropy generation rate caused by time-averaged movements and velocity fluctuations, respectively. Thus, $\dot{S}''_{\bar{D}}$ and $\dot{S}''_{D'}$ represent viscous and turbulent dissipation, respectively. The two terms can be expressed by:

$$\begin{aligned}\dot{S}''_{\bar{D}} = {} & \frac{2\mu}{T}\left[\left(\frac{\partial\bar{u}}{\partial x}\right)^2 + \left(\frac{\partial\bar{v}}{\partial y}\right)^2 + \left(\frac{\partial\bar{w}}{\partial z}\right)^2\right] \\ & + \frac{\mu}{T}\left[\left(\frac{\partial\bar{u}}{\partial y} + \frac{\partial\bar{v}}{\partial x}\right)^2 + \left(\frac{\partial\bar{u}}{\partial z} + \frac{\partial\bar{w}}{\partial x}\right)^2 \right. \\ & \left. + \left(\frac{\partial\bar{v}}{\partial z} + \frac{\partial\bar{w}}{\partial x}\right)^2\right],\end{aligned} \tag{10}$$

$$\begin{aligned}\dot{S}''_{D'} = {} & \frac{2\mu_{ef}}{T}\left[\left(\frac{\partial u'}{\partial x}\right)^2 + \left(\frac{\partial v'}{\partial y}\right)^2 + \left(\frac{\partial w'}{\partial z}\right)^2\right] \\ & + \frac{\mu_{ef}}{T}\left[\left(\frac{\partial u'}{\partial y} + \frac{\partial v'}{\partial x}\right)^2 + \left(\frac{\partial u'}{\partial z} + \frac{\partial w'}{\partial x}\right)^2 \right. \\ & \left. + \left(\frac{\partial v'}{\partial z} + \frac{\partial w'}{\partial x}\right)^2\right],\end{aligned} \tag{11}$$

where $\bar{u}, \bar{v}, \bar{w}$ and $u', v', w'$ represent the mean and fluctuating velocity quantities along $x$, $y$, $z$ direction, respectively. $\mu_{ef}$ denotes effective viscosity and can be defined as:

$$\mu_{ef} = \mu + u_t, \tag{12}$$

where $\mu$ and $\mu_t$ represent molecular and turbulent viscosity, respectively. Through the postprocessing of CFD POST, the term $\dot{S}''_{\bar{D}}$ can be calculated directly by Equation (10). But we cannot obtain the term $\dot{S}''_{D'}$ directly, and the reason is that fluctuating velocities are not available during simulations. Refer to studies of Kock et al. [35, 36], when using SST $k$-$\omega$ turbulence model, $\dot{S}''_{D'}$ can be expressed by:

$$\dot{S}''_{D'} = \alpha\frac{\rho\omega k}{T}, \tag{13}$$

where $\alpha = 0.09$, $\omega$ is characteristic frequency, and $k$ is turbulence kinetic energy. Besides, the overall entropy generation rate of a region is calculated by the volume integration of specific entropy generation rate:

$$\dot{S_{\bar{D}}} = \int_V \dot{S}''_{\bar{D}}\, dV, \tag{14}$$

$$\dot{S_{D'}} = \int_V \dot{S}''_{D'}\, dV, \tag{15}$$

$$\dot{S_D} = \dot{S_{\bar{D}}} + \dot{S_{D'}}, \tag{16}$$

where $\dot{S}_{\bar{D}}$ and $\dot{S}_{D'}$ represent the overall entropy generation rates caused by time-averaged movements and velocity fluctuations, respectively. $\dot{S}_D$ denotes the entropy generation rate of the domain, as the sum of $\dot{S}_{\bar{D}}$ and $\dot{S}_{D'}$. Then, parameters about entropy generation can be calculated for cavitation flows in the pump. With the help of entropy generation method, we can have the quantitative analysis of mechanical energy dissipation.

*3.3. Calculation Domain and Meshing Technique.* The calculation domain is the whole flow passage, which consists of the impeller, diffuser, and other parts, as seen from Figure 3. The lengths of the inlet and outlet pipe are set as 10 times of pipe diameter. Only part impeller is the rotating component while others are stationary. The sliding interfaces are set at split planes of part impeller, as shown in the following figure.

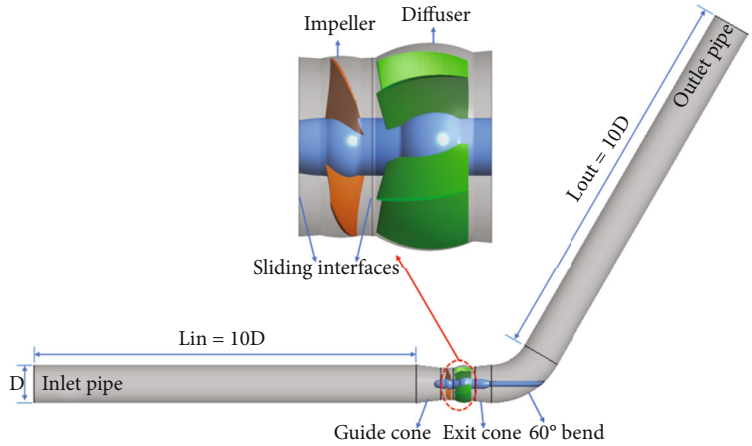


Figure 3: 3D view of calculation domain.

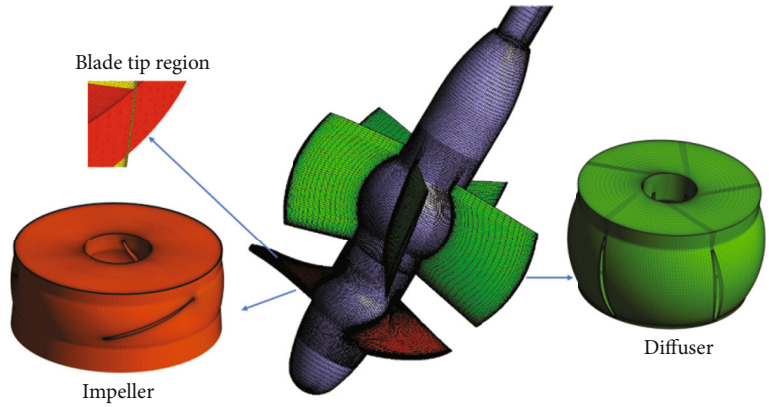


Figure 4: Mesh of main parts for the pump.

Table 2: Grid independence verification.

| Mesh nodes | $Q$ (kg/s) | NPSH (m) | Convergence criterion | Numerical simulation head (m) | Relative error between simulations and experiments |
|---|---|---|---|---|---|
| 3004495 | 302.917 | 9.280 | $10^{-5}$ | 3.885 | 5.937% |
| 4047425 | 302.917 | 9.280 | $10^{-5}$ | 3.981 | 3.668% |
| 5136088 | 302.917 | 9.280 | $10^{-5}$ | 4.008 | 3.024% |
| 6036526 | 302.917 | 9.280 | $10^{-5}$ | 4.014 | 2.864% |

In order to have better convergence, structured hexahedral meshing scheme is applied for all components in the calculation domain. Most meshes are created by software ANSYS ICEM except the mesh of part Impeller. Considering the highly distorted shape of impeller's blades and small radial clearance between blades and the shroud, the mesh of part impeller is created by the software ANSYS TURBOGRID, especially for the O-Grid around blades. In order to simulate the tip region accurately, the tip clearance with a size of 1.2 mm is placed 80-layer mesh grids at the tip. For other tip clearances, the simulation model uses a uniform tip gap with a size of 1.2 mm. To generalize the results and discussions, we should convert the tip clearance size to a fraction of span. Then, 0.15, 0.45, 0.9, and 1.2 mm can be changed to 0.1%, 0.3%, 0.6%, and 0.8% span through dividing by the impeller diameter in the following. The obtained mesh of main parts for the pump is displayed in Figure 4.

Table 3: Comparison between simulations and tests.

| NPSH (m) | Simulation head (m) | Experimental head (m) | Relative error between simulations and tests |
|---|---|---|---|
| 11.531 | 3.915 | 4.027 | 2.786% |
| 9.280 | 4.008 | 4.133 | 3.024% |
| 7.456 | 3.996 | 4.058 | 1.537% |

For the whole calculation domain, four sets of mesh are created, and the verification of grid independence is conducted under specific flow rate and cavitation condition

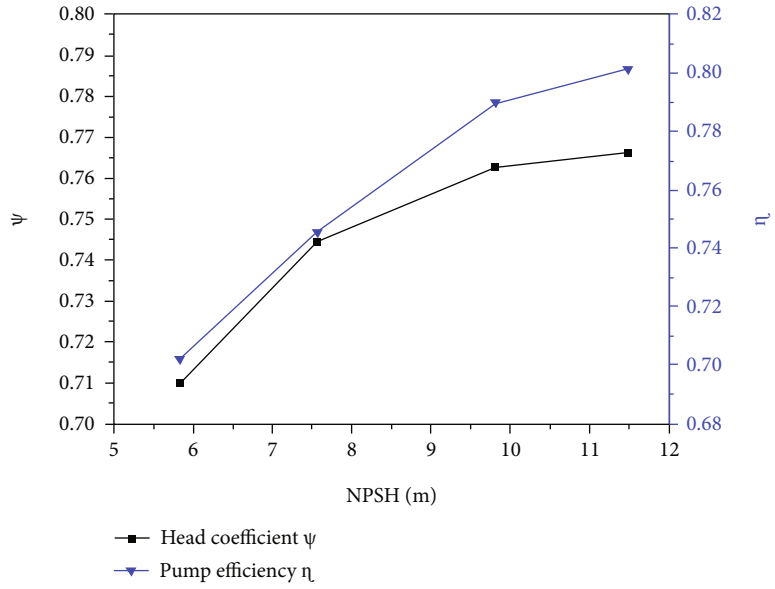


Figure 5: Pump performance with varying NPSH under the tip clearance of 0.1% span.

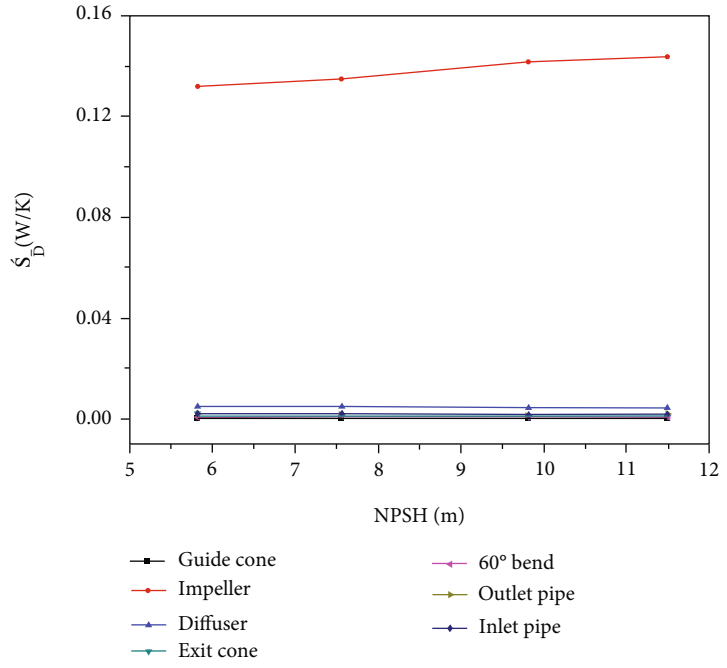


Figure 6: Overall entropy generation rate caused by time-averaged movements $\dot{S}_{\bar{D}}$ for different components.

according to the experiment as displayed in Table 2. The NPSH is an important physical parameter that describes the pump cavitation condition, which can be calculated by:

$$\mathrm{NPSH} = \frac{p_s}{\rho g} + \frac{v_s^2}{2g} - \frac{p_v}{\rho g}, \tag{17}$$

where $p_s$ denotes the absolute pressure, $v_s$ represents the average velocity at the pump inlet, and $p_v$ represents the vapour pressure. SST $k$–$\omega$ turbulence model is taken into consideration for the grid independence study. Through grid independence verification displayed in Table 2, we consider that the number of 5,136,088 nodes is sufficient to simulate cavitation flows in this pump.

*3.4. Numerical Setup.* In this research, 3D transient calculations of the internal flow for different cavitation conditions within an axial-flow pump were conducted applying software ANSYS CFX accompany with the RANS equation. In the calculation, SST $k$-$\omega$ turbulence model and ZGB cavitation model were used. The finite volume method was adopted to discretize govern equations. The second-order upwind scheme was applied for space discretization. For

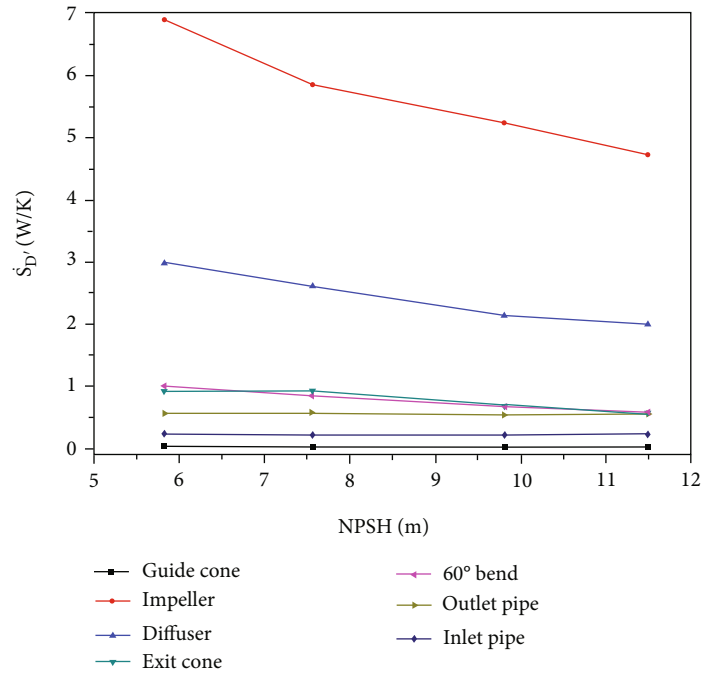


Figure 7: Overall entropy generation rate caused by velocity fluctuations $\dot{S}_{D'}$ for different components.

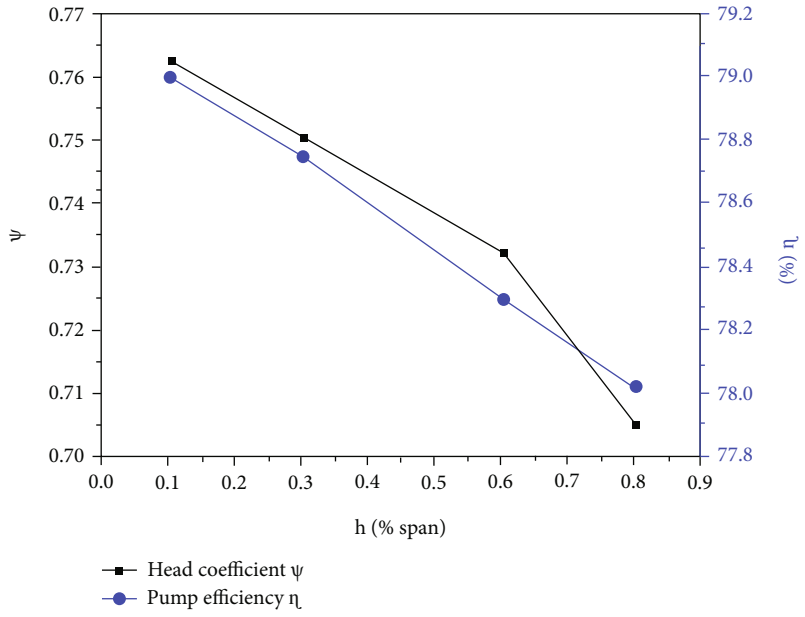


Figure 8: Pump performance for varying tip clearance under NPSH = 9.816 m.

advection terms, the high-resolution scheme with second order backward Euler algorithm was applied. The inlet boundary condition was set as the total pressure inlet; the outlet boundary condition was set as the mass flow rate outlet according to the test data. The wall boundary was assumed for no-slip wall. The calculated media were liquid and vapor at 25°C, and the volume fraction of liquid and vapor was set as 1 and 0 at the pump inlet. The transient rotor stator was employed for the rotor stator interaction. For simulations, steady calculations of noncavitation were first performed, and then, we applied these noncavitation flow results as the initial value to calculate unsteady simulations under cavitation conditions. The convergence criterion was set as $10^{-5}$. For unsteady calculations, the time step was set to 0.0003448276 s, which is equivalent to 1/120 of the design rotational period. During every time step, the maximum number of iterations was assumed as 20 that can generally help the result reach stable periodicity. The total calculation time for unsteady calculations was set to 20 rotating cycles. For analysis, we select the last four periods as our time sample. All results that we used for analysing are based on this average result of the time sample.

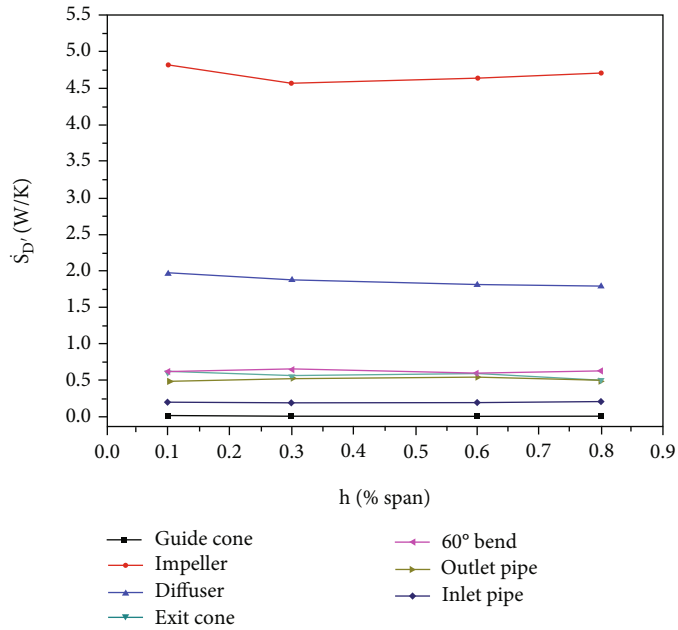


Figure 9: Overall turbulent entropy generation rate $\dot{S}_{D'}$ of different components for varying tip clearance under NPSH = 9.816 m.

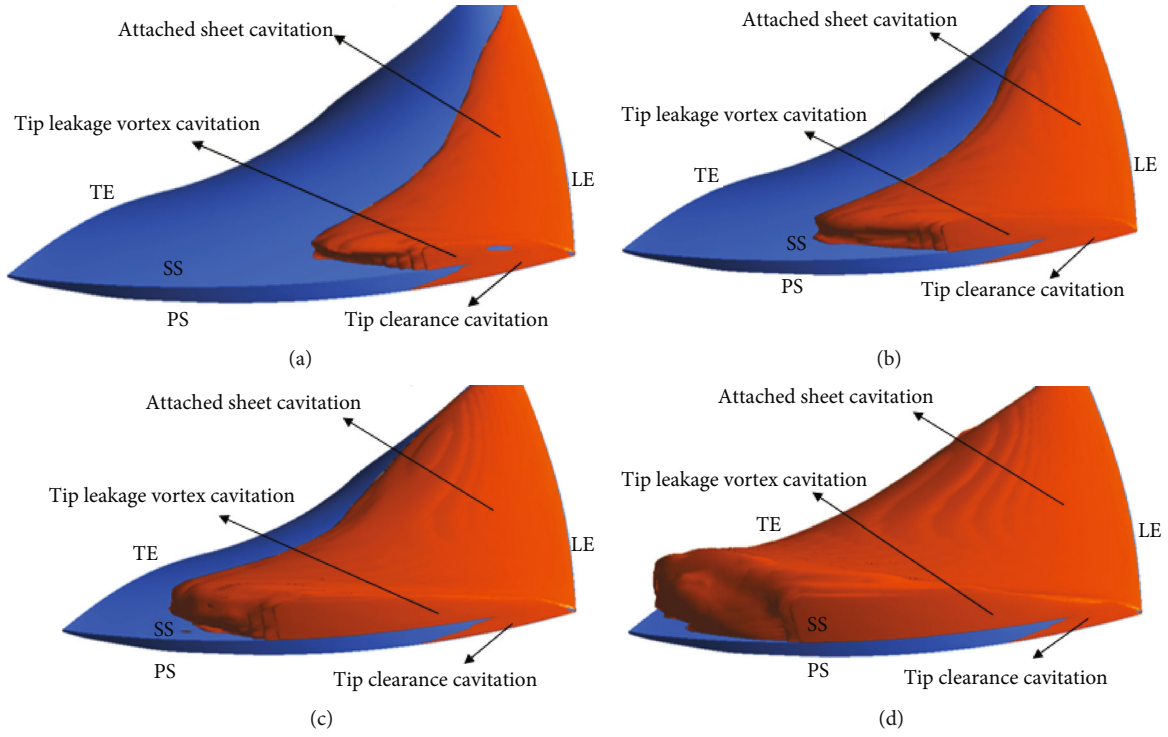


Figure 10: Cavitation patterns with varying NPSH under the tip clearance of 0.1% span. Iso-surface of vapor volume fraction ($\alpha_v = 0.1$) ((a) NPSH = 11.492 m; (b) NPSH = 9.816 m; (c) NPSH = 7.562 m; (d) NPSH = 5.830 m).

*3.5. Validation of Numerical Simulations.* Table 3 shows the comparison of the pump head between experiments and numerical simulations. As displayed in Table 3, the simulation data under three different NPSH are in good agreement with the test data. And the relative error between them is below 5%. Thus, we believe that the model, grid, and calculation method adopted in this research are reasonable and reliable. And we consider the results of simulations can be used for the following analysis.

## 4. Results and Discussion

*4.1. Analysis of Pump Performance and Entropy Generation with Varying NPSH.* During the experiment, it is difficult

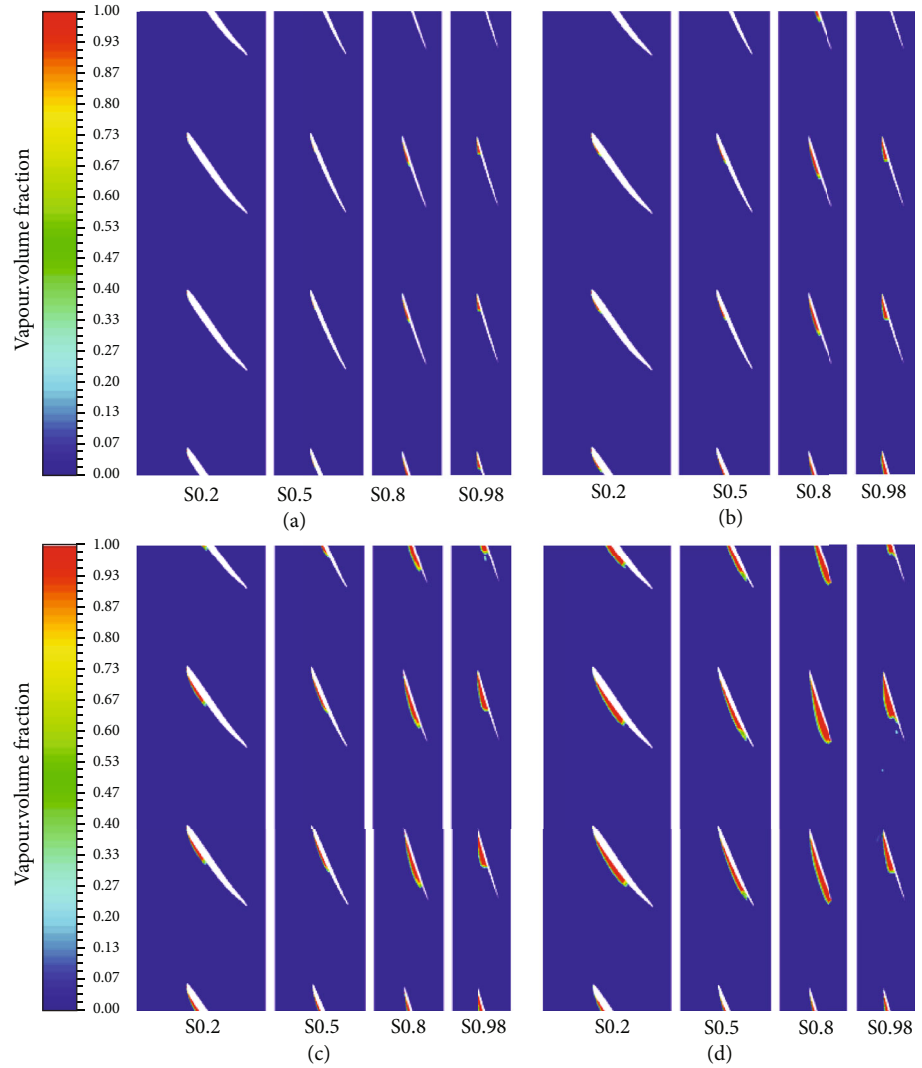


Figure 11: The vapor volume fraction at different spans of part impeller with varying NPSH under the tip clearance of 0.1% span ((a) NPSH = 11.492 m; (b) NPSH = 9.816 m; (c) NPSH = 7.562 m; (d) NPSH = 5.830 m).

to keep the flow rate unchanged when we change the pressure of pump inlet by the vacuum pump; thus, the above simulation results according to the experimental data just adopted for verifying the reliability of simulations. For the following analysis, we use the same conditions except for the analysis variable. To investigate the pump performance and entropy generation with varying NPSH, we select four cavitation points that are similar to the experiment cavitation conditions A (NPSH = 11.492 m), B (NPSH = 9.816 m), C (NPSH = 7.562 m), and D (NPSH = 5.830 m) under the same flow rate ($Q = 302.917$ kg/s) and the tip clearance of 0.1% span for detailed analysis. The calculated pump performance is shown in Figure 5. The nondimensional parameters are calculated by:

$$\text{head coefficient} : \psi = \frac{gH}{(\Omega/2\pi)^2 D^2}, \tag{18}$$

$$\text{pump coefficient} : \eta = \frac{gQH}{3600M\Omega}. \tag{19}$$

As seen from Figure 5, the pump head and efficiency both reduce with the NPSH reducing, which indicates that there will be more energy loss when the cavitation becomes more severe. To better understand the energy dissipation distribution under different NPSH in the axial-flow pump, we calculate the overall entropy generation rate caused by time-averaged movements and velocity fluctuations of different components for analysis, as displayed in Figures 6 and 7. From Figure 6, the entropy generation rates caused by time-averaged movements $\dot{S}_{\bar{D}}$ of different components are very small and change not evidently with varying NPSH. From Figure 7, it is obviously seen that the overall entropy generation rate $\dot{S}_{D'}$ for different components grows from part guide cone, inlet pipe, outlet pipe, 60° bend, exit cone, diffuser, to part impeller. With the NPSH decreasing, the overall entropy generation rate $\dot{S}_{D'}$ of part impeller and diffuser increase obviously while the values for other components remain stable and small. And the overall turbulent entropy generation rate for 60° bend and exit cone increase slowly with the NPSH reducing. Comparing

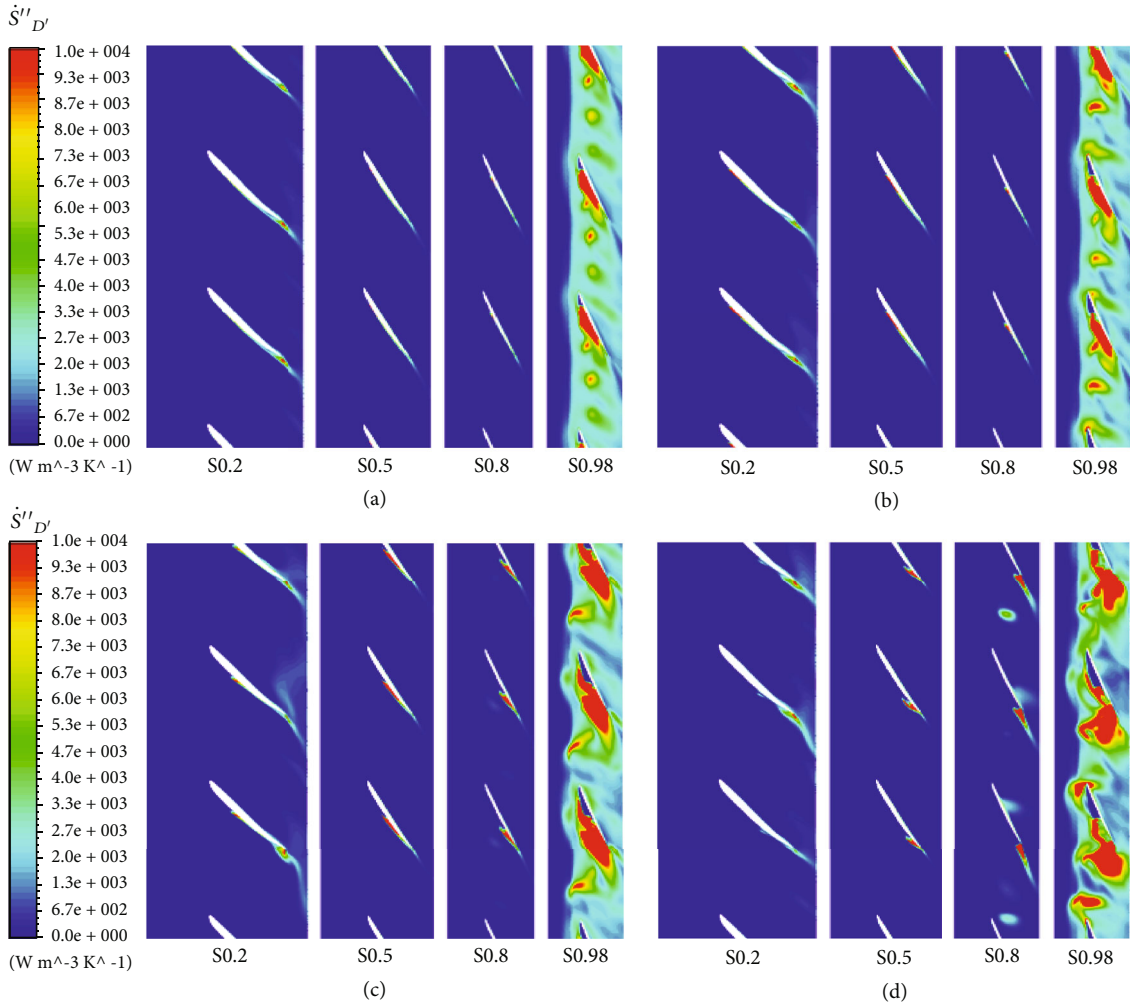


FIGURE 12: Distributions of turbulent entropy generation rate $\dot{S}''_{D'}$ at different spans of part impeller with varying NPSH under the tip clearance of 0.1% span ((a) NPSH = 11.492 m; (b) NPSH = 9.816 m; (c) NPSH = 7.562 m; (d) NPSH = 5.830 m).

the values in Figures 6 and 7, we found that most of the irreversible energy loss are turbulent dissipation; thus, we would focus on the analysis of turbulent dissipation behind. As seen from Figure 7, we found that part impeller and diffuser are main places where the irreversible energy loss occurs, and energy dissipation of part impeller is more than double of the energy dissipation of part diffuser. In a pump, the dissipation of part impeller accounts more than 50% and become bigger with the cavitation being worse. Therefore, the NPSH has significant effects on the turbulent dissipation for part impeller.

*4.2. Analysis of Pump Performance and Entropy Generation with Varying Tip.* When pumps operate, tip clearance between the blade and the impeller's shroud is inevitable. To study impacts of tip clearance width on the pump performance and entropy generation, we select four tip clearance width with the same cavitation (NPSH = 9.816 m) for the following analysis. Figure 8 displays pump performance with four tip clearances under the same cavitation condition, and we can observe that pump head and pump efficiency both reduce as the tip increasing from 0.1% span to 0.8% span. Meanwhile, the difference between the maximum and minimum head is less than 6%, and the difference between the maximum and minimum pump efficiency is about 1%. This indicates that as the tip grows from 0.1% span to 0.8% span under same cavitation condition (NPSH = 9.816 m), the pump performance decreases slightly.

Through the above analysis in Section 4.1, we know most of energy dissipation is turbulent dissipation, thus here mainly analyze the turbulent entropy generation within this pump. Figure 9 displays overall turbulent entropy generation rate $\dot{S}_{D'}$ of different components with varying tip under the same cavitation condition (NPSH = 9.816 m). From Figure 9, it is obviously observed that $\dot{S}_{D'}$ for different components grows from part guide cone, inlet pipe, outlet pipe, 60° bend, exit cone, diffuser, to part impeller. As the tip increases, the overall turbulent entropy generation rates of part impeller first decreases a little then increase slowly, and the changing of the value is not big. While overall entropy generation rate of part diffuser reduces very slowly when the tip increases. And the turbulent entropy generation rate of other components

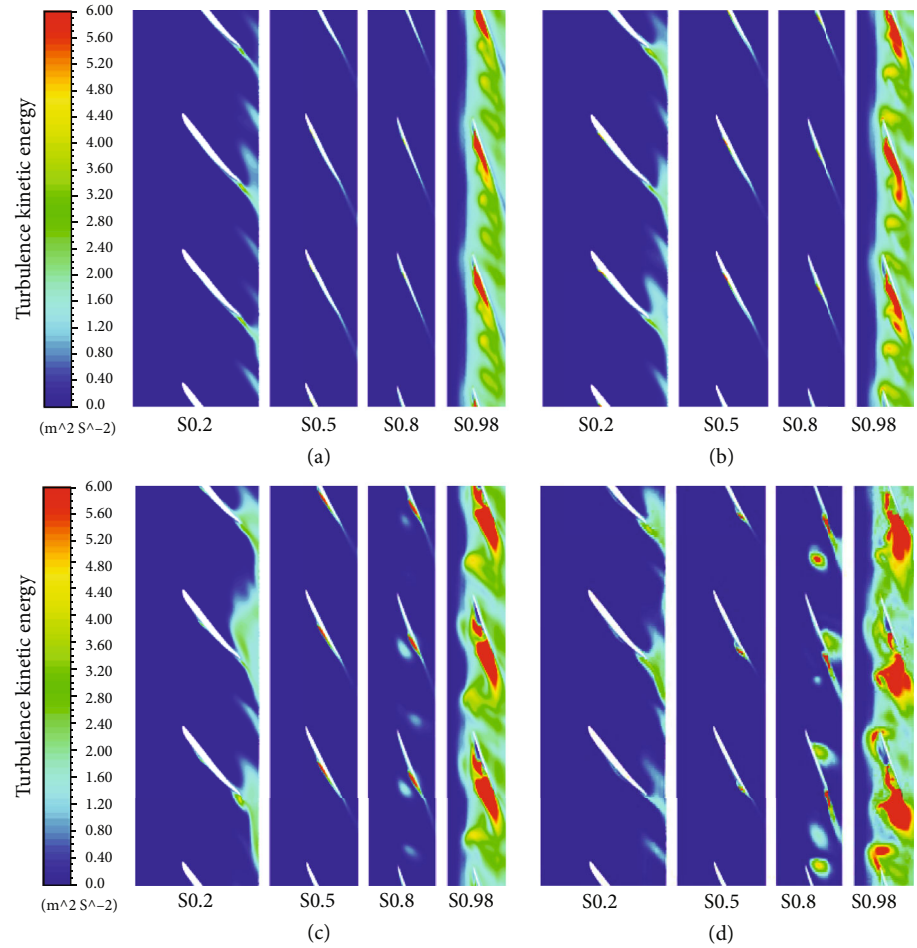


Figure 13: Distributions of turbulence kinetic energy at different spans of part impeller with varying NPSH under the tip clearance of 0.1% span ((a) NPSH = 11.492 m; (b) NPSH = 9.816 m; (c) NPSH = 7.562 m; (d) NPSH = 5.830 m).

remains small and fluctuates in a very small range as the tip increases. From Figure 9, we found that part impeller and diffuser are still main location that irreversible energy loss happens, and the turbulent dissipation of part impeller is more than double of the dissipation of part diffuser. Therefore, the impeller is still the largest place that irreversible energy loss occurs with varying tip. And the tip clearance has a little impact on turbulent dissipation of part impeller.

*4.3. Cavitation Patterns and Entropy Generation Distributions with Varying NPSH.* When axial-flow pumps operate under cavitation conditions, lower pressure generally is located at leading edges of blades' suction sides near part impeller's shroud; thus, the cavitation generally occurs around blade suction surfaces of the impeller. Meanwhile, the impeller has the largest energy dissipation for this axial-flow pump, and most are turbulent dissipation based on the above analysis. Therefore, we here mainly study the cavitation patterns and detailed turbulent entropy generation rate distributions for part impeller. To study the impacts of NPSH on cavitation patterns and entropy generation distributions, we fix the flow rate to 302.917 kg/s and the tip clearance to 0.1% span. Figure 10 shows the cavitation pattern, with iso-surface of vapor volume fraction ($\alpha_v = 0.1$) with varying NPSH for the impeller. Displayed in Figure 10, the cavitation mainly consists of the attached sheet cavitation, tip leakage vortex cavitation, and tip clearance cavitation. Among them, attached cavitation on blades' suction sides and tip leakage vortex cavitation are caused due to pressure difference between pressure and suction sides of blades, and tip clearance cavitation is caused by tip corner vortex on the tip. These types of cavitation also have been validated applying the PIV experiment and simulations [18]. For severe cavitation conditions, different types of cavitation can merge into a large-scale cavitation cloud and block the flow passage in part impeller, then finally decreasing the pump performance. As seen from Figure 10, the red regions of attached sheet cavitation and tip leakage vortex cavitation both increase greatly as NPSH decreases from 11.492 m to 5.83 m. While the red areas of tip clearance cavitation attached on the blade tip surface has no significant changes, this may be due to the smallest tip clearance of 0.1% span. With the NPSH reducing displayed in Figure 10, the attached sheet cavitation extends from first covering less than half of the blade's suction surface in Figure 10(a) to almost covering the entire blade suction tip side in Figure 10(d). Meanwhile, attached sheet cavitation region develops thicker and induces the blockage for the

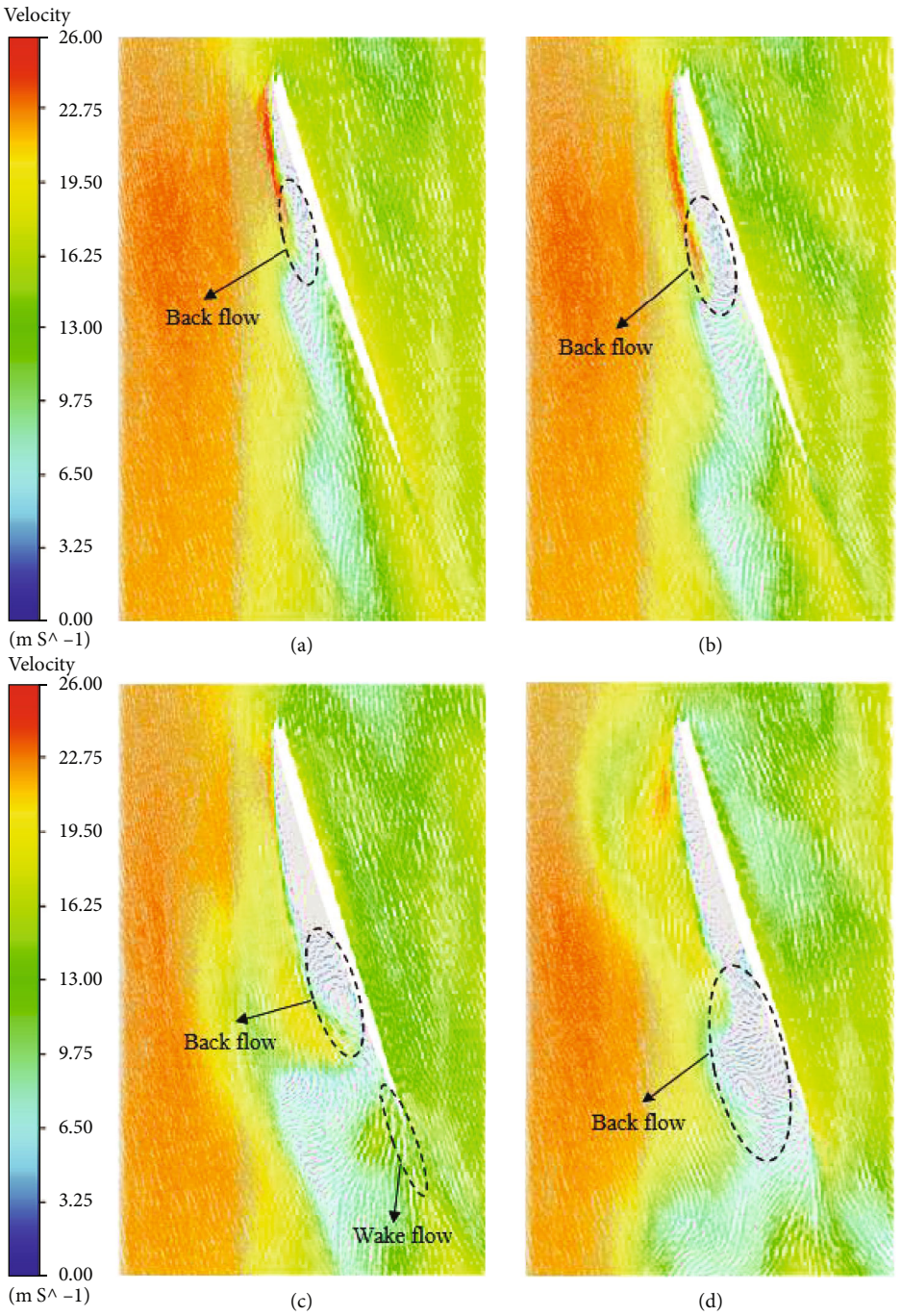


Figure 14: Velocity vector at S0.98 of part impeller with varying NPSH under the tip clearance of 0.1% span ((a) NPSH = 11.492 m; (b) NPSH = 9.816 m; (c) NPSH = 7.562 m; (d) NPSH = 5.830 m).

impeller's channel with the NPSH reducing. From the Figure 10, the tip leakage vortex cavitation connects with attached cavitation, the location at which leakage vortex cavitation leaves from the blade near the shroud moves downstream. Thus, the NPSH has significant effects on the cavitation patterns of the impeller.

To study the relations between the cavitation development and energy dissipation in part impeller with varying NPSH, we here draw the contours of vapor volume fraction at different spans of part impeller as shown in Figure 11 and its corresponding contours of turbulent entropy generation distributions at different spans as shown in Figure 12 to conduct the analysis. The span from hub to shroud is set as 0~1, and S0.98 is close to the shroud. Figure 11 displays vapor volume fraction at varying span (S0.2, S0.5, S0.8, and S0.98) of part impeller under varying NPSH. As seen from Figure 11(a), the areas of cavity mainly emerge near blades' suction sides, with S0.8 and S0.98 having large cavity areas. When the NPSH reduces to 9.816 m as shown in Figure 11(b), the cavity areas extend larger along the blade

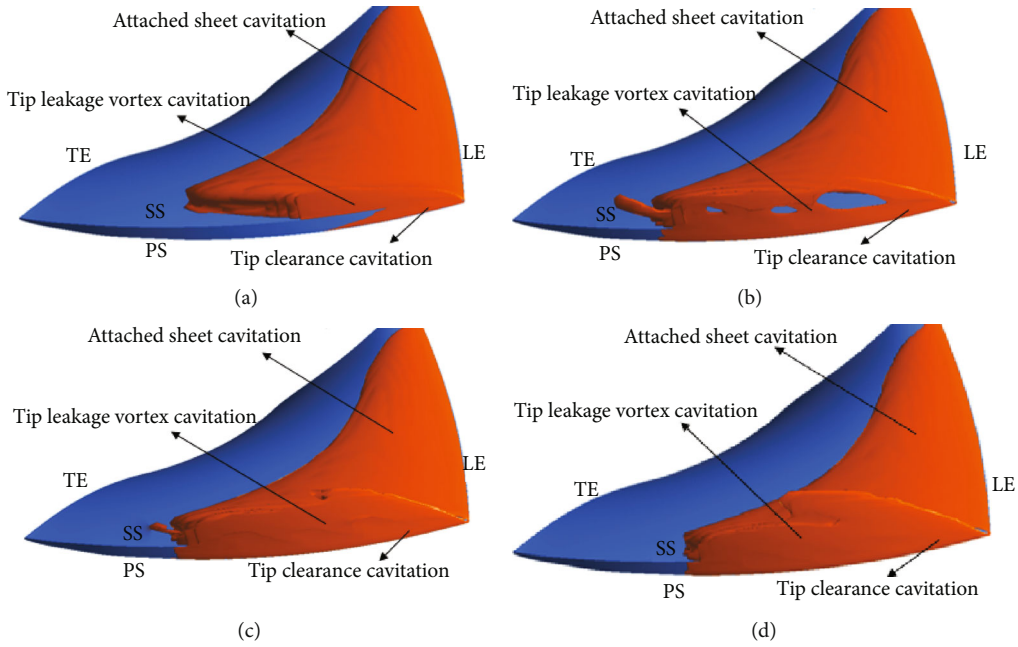


FIGURE 15: Cavitation patterns with varying tip clearance under NPSH = 9.816 m. Iso-surface of vapor volume fraction ($\alpha_v = 0.1$) ((a) $h$ = 0.1% span; (b) $h$ = 0.3% span; (c) $h$ = 0.6% span; (d) $h$ = 0.8% span).

suction side than that shown in Figure 11(a) for each corresponding span especially for span S0.8 and S0.98. When the NPSH further drops from 9.816 m to 5.83 m that changing from Figure 11(b) to Figure 11(d), the cavity areas increase obviously for every corresponding span, which is similar with the variation trend in Figure 10. Thus, the cavity areas of the impeller extend larger along the blade's suction side with NPSH decreasing.

Figure 12 displays distributions of turbulent entropy generation rate $\dot{S}_{D'}''$ in part impeller at varying span (S0.2, S0.5, S0.8, and S0.98) under varying NPSH. Detailed turbulent entropy generation rate distributions can help us determine the locations and magnitude of energy dissipation intuitively and quantitatively. As seen from Figure 12(a), the high regions of $\dot{S}_{D'}''$ most happen near suction surfaces of blades, with S0.98 having largest turbulent dissipation. Through comparing Figure 11 with Figure 12, we observe that the cavitation development has a strong relation with turbulent entropy generation distributions of part impeller. The relation reflects on the field that the high regions of turbulent entropy generation are generally concentrated on the rear part of the cavity for every corresponding span of the impeller. When the NPSH decreases to 9.816 m displayed in Figure 12(b), the distributions of turbulent generation rate are similar with the phenomena displayed in Figure 12(a), but the high areas of $\dot{S}_{D'}''$ at span S0.98 extend larger than that displayed in Figure 12(a). As the NPSH further decreases to 7.562 m displayed in Figure 12(c), the large regions of $\dot{S}_{D'}''$ expand larger along the blade's suction side for each corresponding span especially for S0.98 than that displayed in Figure 12(b). As the NPSH drops to 5.83 m displayed in Figure 12(d), the high areas of $\dot{S}_{D'}''$ extend farther along the blade suction side for S0.98 and other corresponding span. The distribution of large turbulent dissipation at S0.98 shown in Figure 12(d) becomes more disorder and moves more downstream of the impeller than that displayed in Figure 12(c). From the analysis above, we can conclude that the turbulent entropy generation rate of part impeller is mainly located at rear part of the cavity and expand along suction surfaces of blades, with S0.98 having higher turbulent dissipation under these cavitation conditions. And the high areas of turbulent dissipation in part impeller expand larger and move downstream along the blade suction side especially for S0.98 with NPSH reducing. For the cavitation development, the cavity areas increase along the blade suction side especially for the span S0.8 and S0.98 with the NPSH decreasing. As for the relation between the cavitation patterns and turbulent dissipation, the cavity areas and high areas of turbulent dissipation both increase especially for the spans near the shroud with the decrease of the NPSH. Besides, the regions of high turbulent dissipation are mainly occurred at the rear part of cavity and trail of the blade for every corresponding span of the impeller, which indicates that the energy dissipation is concentrated on the rear part of the cavity and the tail of the blade. To study the reason why the high turbulent dissipation gathers in these places, we draw their corresponding contours of turbulence kinetic energy at varying span (S0.2, S0.5, S0.8, and S0.98) of part impeller displayed in Figure 13 to analyze. Through the comparison between the turbulence kinetic energy distributions in Figure 13 and distributions of turbulent entropy generation in Figure 12, we can observe that the regions of large turbulence kinetic energy also have high turbulent entropy generation rate. To deeply investigate the reason for large turbulence kinetic energy near the shroud, here, draw velocity vector on S0.98 under different NPSH with a tip clearance of 0.1% span shown in Figure 14 to analyze. In Figure 14, there is a backflow area at the rear part of the

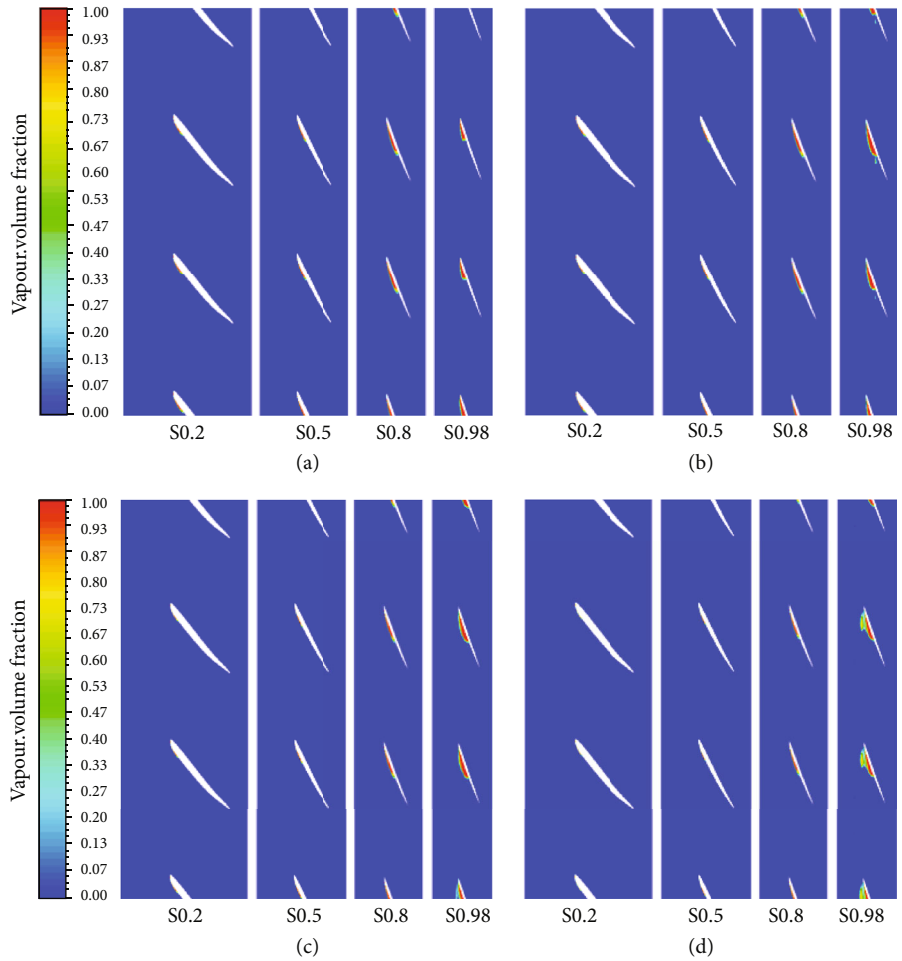


Figure 16: The vapor volume fraction at different spans in part impeller for varying tip clearance under NPSH = 9.816 m ((a) $h = 0.1\%$ span; (b) $h = 0.3\%$ span; (c) $h = 0.6\%$ span; (d) $h = 0.8\%$ span).

cavity and a wake area at the tail of blade, and the backflow area moves downstream and expands along blades' suction sides with the NPSH declining. When the thickness of the backflow area gets close to the thickness of the rear of the cavity, the cavity trail would no longer attach to the blade suction side. When large scale of tail part of the cavity shed from blades, the unsteadiness of the flow increases and high turbulence kinetic energy are generated there. Thus, the unstable flows caused by the rear of the cavity shedding and wake flows are generated at the rear part of the cavity and tail part of the blade, then gathering high turbulence kinetic energy of these areas and finally resulting in large turbulent dissipation there. Therefore, the turbulent dissipation has a close relationship with the cavitation pattern for part impeller. And NPSH has significant impacts on the cavitation development and turbulent dissipation especially the span near part impeller's shroud.

*4.4. Cavitation Patterns and Entropy Generation Distributions with Varying Tip Clearance.* To study impacts of tip clearance on cavitation patterns and entropy generation distributions for the impeller, we fix the NPSH to 9.816 m and flow rate to 302.917 kg/s. Similar to the above analysis, the cavitation patterns by iso-surface of vapor volume fraction ($\alpha_v = 0.1$) with varying tip clearance for the impeller are shown in Figure 15. Also from Figure 15, the cavitation mainly includes the attached sheet cavitation, tip leakage vortex cavitation, and tip clearance cavitation. With the tip increasing from 0.1% span to 0.3% span from Figure 15(a) to Figure 15(b), the red areas of tip leakage vortex cavitation and tip clearance cavitation attached on the blade tip increase obviously under the same NPSH = 9.816 m, while the areas of attached sheet cavitation on blade suction surface change less obviously with the tip increasing from 0.1% span to 0.3% span. Meanwhile, the tip leakage vortex cavitation connects with attached cavitation, the location at which leakage vortex cavitation leaves from blade suction side near the shroud moving downstream as the tip growing from 0.1% span to 0.3% span. With the tip increasing further from 0.3% span to 0.6% span, regions of tip leakage vortex cavitation change from a cavity with holes in Figure 15(b) to a solid and larger cavity that thickens nearer the impeller's inlet in Figure 15(c). Meanwhile, the location at which tip leakage vortex cavitation detaches from the blade suction surface near the shroud changes not evidently with tip clearance growing from 0.3% span to 0.6%

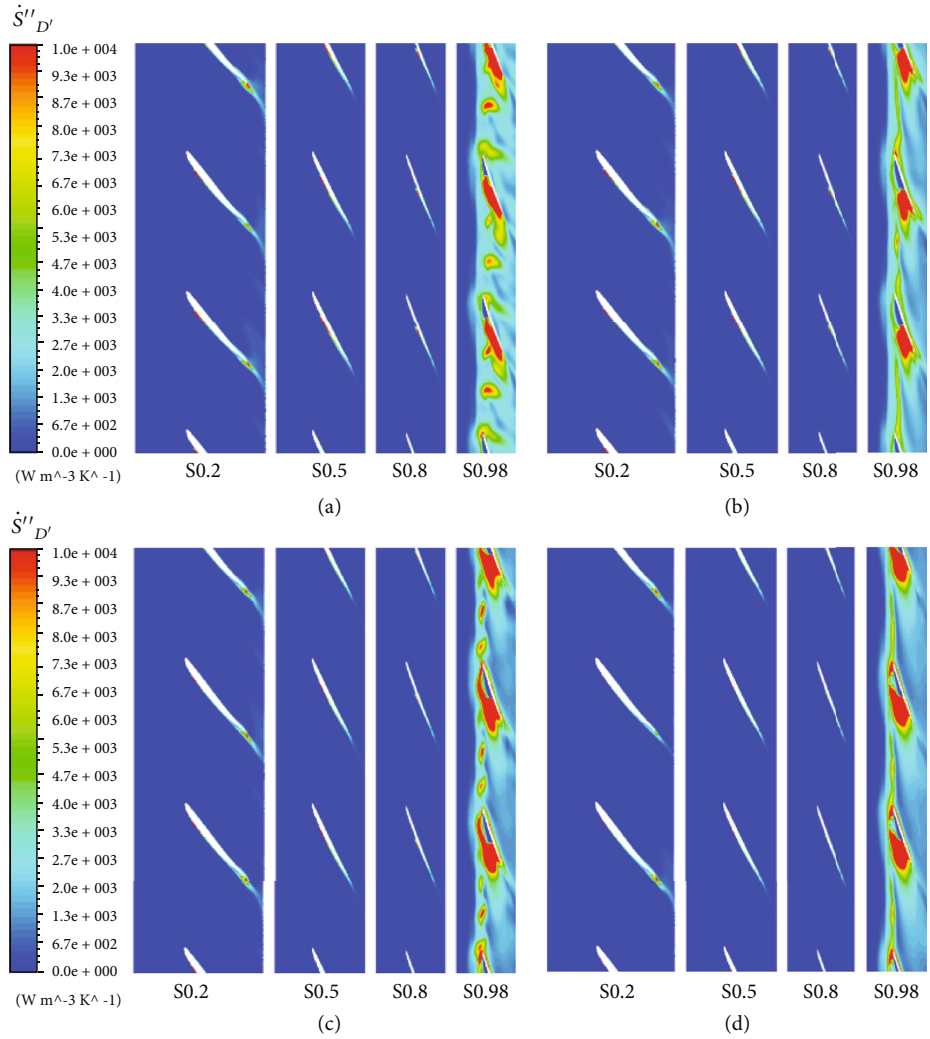


FIGURE 17: Distributions of turbulent entropy generation rate $\dot{S}''_{D'}$ at different spans in part impeller for varying tip clearance under NPSH = 9.816 m ((a) $h = 0.1\%$ span; (b) $h = 0.3\%$ span; (c) $h = 0.6\%$ span; (d) $h = 0.8\%$ span).

span. And areas of tip clearance cavitation that attached on blade tip surface have not evident changes with the growth of the tip from 0.3% span to 0.6% span. As the tip gets to 0.8% span, regions of tip leakage vortex cavitation expand larger, moving more toward the impeller inlet as shown in Figure 15(d) than that as shown in Figure 15(c). Also, the location at which tip leakage vortex cavitation detaches from blades and areas of tip clearance cavitation have not evident changes as the tip growing from 0.6% span to 0.8% span. All in all, we can conclude that the tip gap alters the pattern of tip leakage vortex cavitation and clearance cavitation under this same NPSH. This indicates that tip clearance mainly effects on cavitation patterns near the shroud for the impeller under the same NPSH = 9.816 m.

Like the analysis above, we here draw the contours of vapor volume fraction and turbulent entropy generation at different spans in part impeller as shown in Figures 16 and 17 to investigate impacts of tip width on the cavitation development and energy dissipation for the impeller. Figure 16 shows the vapor volume fraction at different spans (S0.2, S0.5, S0.8, and S0.98) of the impeller with varying tip clearance under the same NPSH = 9.816 m. Figure 16(a) is the same with Figure 11(b), and the areas of cavity mainly occur near the blades' suction surfaces especially for the span S0.8 and S0.98. When the tip increases to 0.3% span displayed in Figure 16(b), regions of the cavity at span S0.98 extend larger along the blade suction side than that displayed in Figure 16(a). As the tip further increases from 0.3% span to 0.8% span that changes from Figure 16(b) to Figure 16(d), the cavity areas mainly change at span S0.98, and the cavity moves more towards the impeller inlet, which is consistent with variation phenomenon in Figure 15. Thus, the increase of tip clearance mainly changes the cavity areas at S0.98 of part impeller. Figure 17 displays the distributions of turbulent entropy generation rate $\dot{S}''_{D'}$ in part impeller at different spans (S0.2, S0.5, S0.8, and S0.98) with varying tip under NPSH = 9.816 m. Figure 17(a) is the same with Figure 12(b), and high regions of $\dot{S}''_{D'}$ are located near the suction surfaces of blades, with S0.98 having larger turbulent dissipation. Through comparing Figure 16 with Figure 17,

we also found that high regions of turbulent entropy generation rate are generally located at the rear part of cavity for every corresponding span of part impeller. As the tip increases from 0.1% span to 0.3% span with same NPSH, high areas of turbulent entropy generation rate at span S0.98 move farther downstream along the blade suction side that seen changing from Figure 17(a) to Figure 17(b). When the tip clearance further increases to 0.6% span displayed in Figure 17(c), the large regions of $\dot{S}''_{D'}$ at span S0.98 extend and move towards the impeller inlet comparing with Figure 17(b). As the tip clearance grows to 0.8% span displayed in Figure 17(d), the areas of high $\dot{S}''_{D'}$ have small changes towards the impeller inlet comparing the high regions of $\dot{S}''_{D'}$ displayed in Figure 17(c). Also, the unstable flows caused by cavity shedding at the rear of the cavity and wake flows at the trail of the blade induce large turbulent dissipation at S0.98 in part impeller. In our current research for the cavitation flows, we conclude that the tip clearance mainly influences the cavitation development and turbulent dissipation distribution around part impeller's shroud under the same NPSH. Meanwhile, the turbulent dissipation has a strong relation with the cavitation pattern for different tip within part impeller, which reflects on the field that high turbulent dissipation is generally located at the rear part of cavity for every corresponding span.

## 5. Conclusions

In the current research, the impacts of different NPSH and tip clearance width on cavitation patterns and energy dissipation in an axial pump are investigated applying numerical simulations with entropy generation method. Through calculating overall entropy generation rate of different parts and analyzing the cavitation patterns and entropy generation distributions for the impeller under varying conditions, we can summarize the following conclusions.

(1) The calculated results indicate that pump performance declines greatly as NPSH reducing with same tip size of 0.1% span, which shows that there are more energy losses when the cavitation becomes more severe. With the tip growing from 0.1% span to 0.8% span under the same cavitation condition (NPSH = 9.816 m), the pump performance decreases slightly. Meanwhile, part impeller and diffuser are mainly places of entropy generation for different NPSH and tip width; part impeller is the component with more than 50% of the dissipation for the entire pump. And most are turbulent dissipation.

(2) As the NPSH decreases from 11.492 m to 5.83 m under the tip clearance of 0.1% span, the regions of attached sheet cavitation and tip leakage vortex cavitation near blades both increase greatly as displayed in Figure 10, while the areas of tip clearance cavitation attached on the blade tip surface have no significant changes. The cavity areas of the impeller extend larger along blade suction side especially for the span S0.8 and S0.98 with the decrease of the NPSH. With the NPSH decreasing, the high regions of dissipation in part impeller expand along the blades and move downstream, with S0.98 having larger turbulent dissipation under the same tip clearance of 0.1% span. Besides, the areas of large turbulent dissipation are mainly located at the rear part of cavity for every corresponding span of the impeller, which indicates that the turbulent dissipation has a relationship with cavitation pattern of part impeller. The unstable flows caused by cavity shedding at the rear of the cavity and wake flows near the blade trail induce high turbulent dissipation of part impeller. Therefore, the change of NPSH has significant impacts on the cavitation development and turbulent dissipation especially for the span near the impeller's shroud.

(3) With the tip growing from 0.1% span to 0.8% span under the same NPSH displayed in Figure 15, the areas of tip leakage vortex cavitation and tip clearance cavitation near the shroud expand along blade suction surface. This indicates that tip clearance mainly effects on cavitation patterns near the shroud for the impeller under the same NPSH. With the tip clearance growing, high regions of turbulent dissipation are mainly distributed along the blade suction sides and move downstream, with the span S0.98 having larger turbulent dissipation. Also, the regions of high turbulent dissipation are mainly occurred at the rear part of cavity for every corresponding span in part impeller. Thus, the tip clearance width mainly influences the cavitation development and turbulent dissipation distributions around part impeller's shroud under the same NPSH.

## Nomenclature

| | |
|---|---|
| $Q$: | Mass flow rate (kg/s) |
| $D$: | Impeller diameter (mm) |
| $H$: | Head (m) |
| $n$: | Rotational speed (r/min) |
| $H_d$: | Design head (m) |
| $Q_d$: | Design flow rate (kg/s) |
| $M$: | Torque ($N * m$) |
| $\Omega$: | Rotor angular velocity (rad/s) |
| $p$: | Pressure (Pa) |
| $g$: | Gravity acceleration ($m/s^2$) |
| $p_v$: | Vapor pressure (Pa) |
| $h$: | Tip clearance width (mm) |
| $\rho$: | Density ($kg/m^3$) |
| $\alpha_v$: | Volume fraction of vapor |
| $\varphi$: | Flow coefficient |
| $\psi$: | Head coefficient |
| $\eta$: | Pump efficiency (%) |
| $\omega$: | Characteristic frequency |
| $\mu$: | Molecular viscosity |
| $\mu_t$: | Turbulent viscosity |
| $k$: | Turbulence kinetic energy ($m^2/s^2$) |
| NPSH: | net positive suction head (m) |

Subscripts $l$, $m$, $v$: Liquid, mixture, vapor
$u$, $v$, $w$: Velocity component along $x$, $y$, $z$ direction (m/s)
$\overline{()}$: Mean component
$()'$: Fluctuating component
LE: Leading edge
TE: Trailing edge
PS: Pressure side
SS: Suction side
$\dot{S}_D''$: Entropy generation rate caused by time-averaged movements ($Wm^{-3}K^{-1}$)
$\dot{S}_{D'}''$: Entropy generation rate caused by velocity fluctuations ($Wm^{-3}K^{-1}$)
$\dot{S}_{\bar{D}}$: Overall entropy generation rate caused by time-averaged movements of a region (W/K)
$\dot{S}_D{}'$: Overall entropy rate caused by velocity fluctuations of a region (W/K)
$\dot{S}_D$: Overall entropy generation rate of a region (W/K).

## Data Availability

All data generated or analyzed during this study are included in this article.

## Conflicts of Interest

The authors declare that they have no conflicts of interest.

## Authors' Contributions

Simin Shen (first author and corresponding author) is responsible for conceptualization, resources, software, methodology, formal analysis, investigation, writing—original draft, and writing—review and editing; Bensheng Huang (second author) for supervision; Si Huang (third author) for supervision and validation; and Shun Xu (fourth author) and Shufeng Liu (fifth author) for funding acquisition.

## Acknowledgments

This research was sponsored by the National Natural Science Foundation of China (NSFC, grant no. 52109104).

## References

[1] S. Gopalan, J. Katz, and H. L. Liu, "Effect of gap size on tip leakage cavitation inception, associated noise and flow structure," *Journal of Fluids Engineering*, vol. 124, no. 4, pp. 994–1004, 2002.

[2] S. Christopher and S. Kumaraswamy, "Identification of critical net positive suction head from noise and vibration in a radial flow pump for different leading edge profiles of the vane," *Journal of Fluids Engineering*, vol. 135, no. 12, 2013.

[3] C. Haosheng, L. Jiang, and L. Shihan, "Thermal effect at the incipient stage of cavitation erosion on a stainless steel in ultrasonic vibration cavitation," *Journal of Fluids Engineering*, vol. 131, no. 2, 2009.

[4] B. Pouffary, R. F. Patella, J. L. Reboud, and P. A. Lambert, "Numerical simulation of 3D cavitating flows: analysis of cavitation head drop in turbomachinery," *Journal of Fluids Engineering*, vol. 130, no. 6, 2008.

[5] S. Saito, "Cavitation aspect and flow pattern in an axial-flow impeller," *Transactions of The Japan Society of Mechanical Engineers*, vol. 53, no. 492, pp. 2483–2491, 1987.

[6] R. Zhang and H. Chen, "Numerical analysis of cavitation within slanted axial-flow pump," *Journal of Hydrodynamics*, vol. 25, no. 5, pp. 663–672, 2013.

[7] K. Hosono, Y. Kajie, S. Saito, and K. Miyagawa, "Study on cavitation influence for pump head in an axial flow pump," *Journal of Physics*, vol. 656, no. 1, p. 012062, 2015.

[8] L. Shi, D. S. Zhang, R. J. Zhao, W. D. Shi, and Y. X. Jin, "Effect of blade tip geometry on tip leakage vortex dynamics and cavitation pattern in axial-flow pump," *Science China Technological Sciences*, vol. 60, no. 10, pp. 1480–1493, 2017.

[9] D. Zhang, L. Shi, W. Shi, R. Zhao, H. Wang, and B. P. M. (Bart) van Esch, "Numerical analysis of unsteady tip leakage vortex cavitation cloud and unstable suction-side-perpendicular cavitating vortices in an axial flow pump," *International Journal of Multiphase Flow*, vol. 77, pp. 244–259, 2015.

[10] D. Zhang, W. Shi, D. Pan, and M. Dubuisson, "Numerical and experimental investigation of tip leakage vortex cavitation patterns and mechanisms in an axial flow pump," *Journal of Fluids Engineering*, vol. 137, no. 12, 2015.

[11] D. Y. Tan, R. L. Miorini, J. Keller, and J. Katz, "Flow visualization using cavitation within blade passage of an axial waterjet pump rotor," *Fluids Engineering Division Summer Meeting*, vol. 44755, pp. 395–404, 2012.

[12] W. Feng, Q. Cheng, Z. Guo, and Z. Qian, "Simulation of cavitation performance of an axial flow pump with inlet guide vanes," *Advances in Mechanical Engineering*, vol. 8, no. 6, 2016.

[13] Z. Qian, F. Wang, Z. Guo, and J. Lu, "Performance evaluation of an axial-flow pump with adjustable guide vanes in turbine mode," *Renewable Energy*, vol. 99, pp. 1146–1152, 2016.

[14] S. Shen, Z. Qian, B. Ji, and R. K. Agarwal, "Numerical investigation of tip flow dynamics and main flow characteristics with varying tip clearance widths for an axial-flow pump," *Proceedings of the Institution of Mechanical Engineers, Part A: Journal of Power and Energy*, vol. 233, no. 4, pp. 476–488, 2019.

[15] Z. Guo, J. Pan, Z. Qian, and B. Ji, "Experimental and numerical analysis of the unsteady influence of the inlet guide vanes on cavitation performance of an axial pump," *Proceedings of the Institution of Mechanical Engineers, Part C: Journal of Mechanical Engineering Science*, vol. 233, no. 11, pp. 3816–3826, 2019.

[16] D. Zhang, W. Shi, B. B. Van Esch, L. Shi, and M. Dubuisson, "Numerical and experimental investigation of tip leakage vortex trajectory and dynamics in an axial flow pump," *Computers & Fluids*, vol. 112, pp. 61–71, 2015.

[17] Y. Liu, L. Tan, Y. Hao, and Y. Xu, "Energy performance and flow patterns of a mixed-flow pump with different tip clearance sizes," *Energies*, vol. 10, no. 2, p. 191, 2017.

[18] H. Wu, R. L. Miorini, and J. Katz, "Measurements of the tip leakage vortex structures and turbulence in the meridional plane of an axial water-jet pump," *Experiments in Fluids*, vol. 50, no. 4, pp. 989–1003, 2011.

[19] Y. Hao and L. Tan, "Symmetrical and unsymmetrical tip clearances on cavitation performance and radial force of a mixed

flow pump as turbine at pump mode," *Renewable Energy*, vol. 127, pp. 368–376, 2018.

[20] L. Shi, D. Zhang, R. Zhao, W. Shi, and B. V. Bpm, "Visualized observations of trajectory and dynamics of unsteady tip cloud cavitating vortices in axial flow pump," *Journal of Fluid Science and Technology*, vol. 12, no. 1, p. JFST0007, 2017.

[21] Y. Liu and L. Tan, "Tip clearance on pressure fluctuation intensity and vortex characteristic of a mixed flow pump as turbine at pump mode," *Renewable Energy*, vol. 129, pp. 606–615, 2018.

[22] D. Li, Z. Ren, R. Fan, Y. Chai, R. Gong, and H. Wang, "Influence of axial clearance on the performance characteristics of a turbo pump," *Journal of Mechanical Science and Technology*, vol. 35, no. 10, pp. 4543–4555, 2021.

[23] R. Z. Gong, H. J. Wang, L. X. Chen, D. Y. Li, H. C. Zhang, and X. Z. Wei, "Application of entropy production theory to hydro-turbine hydraulic analysis," *Science China Technological Sciences*, vol. 56, no. 7, pp. 1636–1643, 2013.

[24] D. Li, H. Wang, Y. Qin, L. Han, X. Wei, and D. Qin, "Entropy production analysis of hysteresis characteristic of a pump-turbine model," *Energy Conversion and Management*, vol. 149, pp. 175–191, 2017.

[25] D. Li, H. Wang, Y. Qin, X. Wei, and D. Qin, "Numerical simulation of hysteresis characteristic in the hump region of a pump-turbine model," *Renewable Energy*, vol. 115, pp. 433–447, 2018.

[26] H. Hou, Y. Zhang, Z. Li, T. Jiang, J. Zhang, and C. Xu, "Numerical analysis of entropy production on a LNG cryogenic submerged pump," *Journal of Natural Gas Science and Engineering*, vol. 36, pp. 87–96, 2016.

[27] J. Pei, F. Meng, Y. Li, S. Yuan, and J. Chen, "Effects of distance between impeller and guide vane on losses in a low head pump by entropy production analysis," *Advances in Mechanical Engineering*, vol. 8, no. 11, 2016.

[28] H. Chang, W. Shi, W. Li, and J. Liu, "Energy loss analysis of novel self-priming pump based on the entropy production theory," *Journal of Thermal Science*, vol. 28, no. 2, pp. 306–318, 2019.

[29] X. Li, Z. Jiang, Z. Zhu, Q. Si, and Y. Li, "Entropy generation analysis for the cavitating head-drop characteristic of a centrifugal pump," *Proceedings of the Institution of Mechanical Engineers, Part C: Journal of Mechanical Engineering Science*, vol. 232, no. 24, pp. 4637–4646, 2018.

[30] C. Wang, Y. Zhang, H. Hou, J. Zhang, and C. Xu, "Entropy production diagnostic analysis of energy consumption for cavitation flow in a two-stage LNG cryogenic submerged pump," *International Journal of Heat and Mass Transfer*, vol. 129, pp. 342–356, 2019.

[31] S. Shen, Z. Qian, and B. Ji, "Numerical analysis of mechanical energy dissipation for an axial-flow pump based on entropy generation theory," *Energies*, vol. 12, no. 21, p. 4162, 2019.

[32] A. Yu, Q. Tang, H. Chen, and D. Zhou, "Investigations of the thermodynamic entropy evaluation in a hydraulic turbine under various operating conditions," *Renewable Energy*, vol. 180, pp. 1026–1043, 2021.

[33] L. Ji, W. Li, W. Shi, H. Chang, and Z. Yang, "Energy characteristics of mixed-flow pump under different tip clearances based on entropy production analysis," *Energy*, vol. 199, p. 117447, 2020.

[34] T. Lin, X. Li, Z. Zhu, J. Xie, Y. Li, and H. Yang, "Application of enstrophy dissipation to analyze energy loss in a centrifugal pump as turbine," *Renewable Energy*, vol. 163, pp. 41–55, 2021.

[35] F. Kock and H. Herwig, "Local entropy production in turbulent shear flows: a high-Reynolds number model with wall functions," *International Journal of Heat and Mass Transfer*, vol. 47, no. 10-11, pp. 2205–2215, 2004.

[36] J. Mathieu and J. Scott, *An Introduction to Turbulent Flow*, Cambridge University Press, 2018.